Mon. Not. R. Astron. Soc. **000**, 000–000 (0000) Printed 4 February 2008 (MN LaTeX style file v2.2)

arXiv:astro-ph/0601421v2 24 Jan 2006

The infrared jet in Centaurus A: multiwavelength constraints on emission mechanisms and particle acceleration

M.J. Hardcastle[1], R.P. Kraft[2] and D.M. Worrall[3]
[1] *School of Physics, Astronomy and Mathematics, University of Hertfordshire, College Lane, Hatfield, Hertfordshire AL10 9AB*
[2] *Harvard-Smithsonian Center for Astrophysics, 60 Garden Street, Cambridge, MA 02138, USA*
[3] *Department of Physics, University of Bristol, Tyndall Avenue, Bristol BS8 1TL*

4 February 2008

ABSTRACT
We report on *Spitzer* and Gemini observations of the jet of Centaurus A in the infrared, which we combine with radio, ultraviolet and X-ray data. *Spitzer* detects jet emission from about 2 arcmin from the nucleus, becoming particularly bright after the jet flare point at ~ 3.4 arcmin. Where X-ray and infrared emission are seen together the broad-band data strongly support a synchrotron origin for the X-rays. The jet flare point is marked by a broad, diffuse region of X-rays which may be associated with a shock: we discuss possible physical mechanisms for this. The infrared jet persists after the flare point region although X-ray emission is absent; it is plausible that here we are seeing the effects of particle acceleration followed by downstream advection with synchrotron losses. Gemini data probe the inner regions of the jet, putting limits on the mid-infrared flux of jet knots.

Key words: galaxies: active – galaxies: individual: Centaurus A – galaxies: jets

1 INTRODUCTION

Centaurus A is the closest radio galaxy (we adopt $D = 3.4$ Mpc, Israel 1998) as well as the closest active galaxy and large elliptical. Its proximity makes it a vital laboratory for AGN studies of all kinds. Its nucleus shows both heavily obscured and unobscured X-ray components (Evans et al. 2004), making it one of the few low-power radio galaxies to show X-ray evidence for the obscuring torus of canonical unification models (Evans et al. 2006). Its X-ray jet, one of the first to be discovered (Schreier et al. 1979) has been studied in great detail with *Chandra* (Kraft et al. 2000, 2002; Hardcastle et al. 2003, hereafter H03; Kataoka et al. 2006). Because of the high spatial resolution (1 arcsec = 17 pc) compared to that available for more typical X-ray jets in more powerful FRI sources, observations of the jet provide evidence for both localized and diffuse particle acceleration processes. Finally, Cen A's SW radio lobe, in expanding through the ISM of the host galaxy, drives what is currently the only clear example of a high Mach number, attached bow shock to be observed in X-rays around a radio galaxy (Kraft et al. 2003).

Cen A's main disadvantage as a subject for broad-band studies is the strong dust lane, which obscures the inner regions of the source in the optical to ultraviolet. Partly as a result of this, and partly because the jet is relatively weak compared to the emission from stars, there have until recently been no clear detections of synchrotron emission from the jet at frequencies between radio and X-ray, although several claims of optical and infrared emission that may be related to the jet or material around it have been made (e.g. Brodie et al. 1983, Joy et al. 1991, Leeuw et al. 2002). This contrasts with the situation in other well-studied low-power jets, such as M87 (e.g. Perlman et al. 2001) or 3C 66B (Hardcastle et al. 2001) in which data in the infrared, optical and ultraviolet support a synchrotron origin and provide constraints on particle acceleration and energy-production processes.

However, recent *Spitzer* observations have detected the jet of Cen A in the mid-infrared (Brookes et al. 2006), while *GALEX* detects it in the ultraviolet (Neff et al. 2003). In this letter we combine these data with new and archival radio and X-ray observations and discuss their implications for particle acceleration processes. In addition, we use observations of the nuclear regions with Gemini at 10 μm to place constraints on the properties of the nucleus and the inner jet.

Except where otherwise stated, spectral indices α are the energy indices, defined in the sense that flux $\propto \nu^{-\alpha}$.

2 OBSERVATIONS

2.1 *Spitzer* data

The *Spitzer* data we used, described in more detail by Brookes et al. (2006), are taken from the public archive, and consist of two datasets, a set of IRAC observations taken on 2004 Feb 10 and a set of MIPS observations taken on 2004 Aug 06. Several sets of MIPS observations are available in the archive: the one we chose to use (AOR 4940288) covers a wide area around the centre of Cen A. The data used were the Post-Basic Calibrated Data (PBCD) files available from the archive. These include an automated, flux-calibrated mosaic ('MAIC' file) of the numerous individual maps that go to make up an observation. The PBCD files are stated in the instrument data handbooks (http://ssc.spitzer.caltech.edu/irac/dh/ ; http://ssc.spitzer.caltech.edu/mips/dh/) to be suitable at the time of writing for basic scientific analysis for all IRAC channels and for the 24-μm channel (channel 1) of the MIPS data. The low angular resolution and calibration issues of the longer-wavelength MIPS channels meant that these were not suitable for our analysis in any case. IRAC channel 1 (3.6 μm) was too dominated by starlight from the host galaxy and from foreground objects to be useful in our analysis. Accordingly, the data we use are from the three remaining IRAC channels, at 4.5, 5.8 and 8.0μm, and from MIPS at 24 μm; Brookes et al. (2006) show a selection of images in these bands. We carried out aperture photometry, using a local background and excluding point sources from source and background regions, to measure flux densities from components of the jet. Our photometry is consistent with the independent analysis of Brookes et al.

2.2 Gemini data

The nuclear regions of Cen A were observed with the T-ReCS instrument on Gemini South at N-band (10 μm) on 2004 Mar 06 and 2004 Mar 11-12. We obtained these observations in an attempt to detect the bright radio and X-ray components of the inner jet, and so the T-ReCS field of view (28.8×21.6 arcsec) was aligned along the jet, with the active nucleus in one corner. The standard nod and chop mode was used for background subtraction, and the baseline calibration was used for photometry and point-spread function (PSF) determination, using observations of standard stars. In total the on-source exposure time was around 2.1 h.

2.3 VLA data

The 8.4-GHz VLA data that we have described in earlier papers (Kraft et al. 2002, H03) were not ideal for comparison with the large-scale *Spitzer* jet because of the VLA's small primary beam at this wavelength. We therefore re-reduced the data described by Clarke et al. (1992) at 1.5 and 4.9 GHz. These are well matched to the angular scales and resolution of the *Spitzer* data. For smaller-scale mapping we used our existing 8.4-GHz data. VLA data from different configurations were calibrated and combined within AIPS, and a primary beam correction was applied to all images.

2.4 *GALEX* data

The *GALEX* data we use were taken from the archive (http://galex.stsci.edu/GR1/) and were derived from observations made on 2003 Jun 07 as part of the Nearby Galaxies Survey, as reported by Neff et al. (2003); Brookes et al. (2006) show an image. Two broad bandpasses are available, with mean wavelengths of 153 and 231 nm. We use the background-subtracted intensity map, with units of (corrected) counts s^{-1}, for our measurements. Photometry was carried out in the same way as for the *Spitzer* data, using ground-based calibration (http://galexgi.gsfc.nasa.gov/Documents/ERO_data_description_2.htm), correcting for a Galactic $E(B-V)$ of 0.114 mag using the extinction curves of Cardelli, Clayton & Mathis (1989), which give correction factors of 0.94 mag at both mean wavelengths. Since the photometric zero point is not yet well defined and the extinction correction varies significantly over the bandpasses, there are potentially large systematic errors in the conversion between GALEX count rate and flux density.

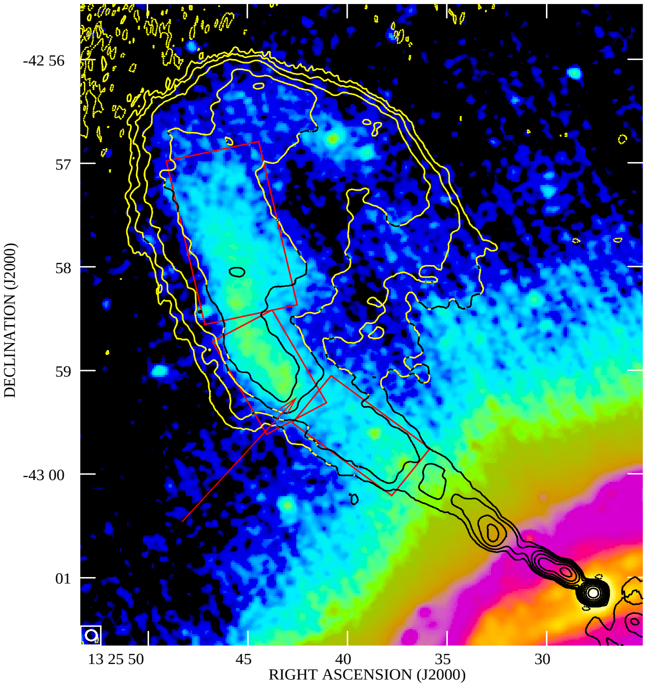

Figure 1. The Cen A jet at 24 μm, using a logarithmic transfer function, with overlaid contours from a 6-arcsec resolution 4.9-GHz radio map. Black is the background level of 32.8 MJy sr^{-1} and the peak is 724 MJy sr^{-1}. The lowest contour is at 0.01 Jy beam^{-1}; contours increase by a factor 2. The flare point (peak surface brightness 33.4 MJy sr^{-1}) is marked with an arrow and the regions used for flux measurement are shown as red boxes.

2.5 *Chandra* data

For the high-energy constraints on the spectrum of the jet we used two *Chandra* datasets taken using the ACIS-S instrument: the observation taken on 2002 Sep 03 (obsid 2978) which was taken as part of the HRC guaranteed time programme, and the observation taken on 2003 Sep 14 (obsid 3965) which was taken by us in guest observer time. These two observations are well matched in position on the instrument and roll angle. The data were reprocessed and filtered using CIAO 3.2.2 and CALDB 3.1 (applying new bad pixel files, removing afterglow detection, and removing the 0.5-arcsec pixel randomization) and were both aligned to the radio core position. After filtering they had livetimes of 44592 and 49518 s respectively, giving a total effective on-source time of 94.1 ks. Spectra were extracted from regions matched to those used at other wavelengths, with local background subtraction, using the *acisspec* tool within CIAO and appropriate response matrices were generated with *mkacisrmf*. Spectral fitting was done within XSPEC 11.3.

3 RESULTS

3.1 The large-scale jet

In the 24-μm data extended emission from the jet is clearly detected from about 2 arcmin (Fig. 1) and extends at least until the end of the clearly defined radio jet. (Two strong infrared point sources in the lobe to the NW of the jet are probably unrelated to it.) The brightest region of the infrared jet, and the part most clearly detected against the higher background in the shorter-wavelength IRAC images, occurs at a region where the radio jet becomes abruptly brighter, and

Table 1. Flux densities from regions of the large-scale jet: see Fig. 1 for regions. Errors are nominal 3 per cent calibration errors (radio), errors based on calibration and background uncertainties (infrared and ultraviolet) or statistical errors (X-ray).

Region	Flux density									
	1.4 GHz (Jy)	4.9 GHz (Jy)	8.4 GHz (Jy)	24 μm (mJy)	8.0 μm (mJy)	5.4 μm (mJy)	4.5 μm (mJy)	231 nm (μJy)	153 nm (μJy)	1 keV (nJy)
Inner	3.25 ± 0.10	1.67 ± 0.05	1.0 ± 0.03	9.0 ± 1.8	–	2.4 ± 0.7	–	80 ± 12	–	27.2 ± 0.3
Middle	9.73 ± 0.30	5.21 ± 0.16	3.79 ± 0.11	15.9 ± 3.1	6.0 ± 1.8	4.9 ± 1.4	3.8 ± 1.1	180 ± 25	70 ± 18	16 ± 0.5
Outer	20.2 ± 0.6	10.1 ± 0.3	–	24.3 ± 4.9	4.2 ± 1.3	5.2 ± 1.6	4.0 ± 1.2	–	–	< 3

starts to bend northwards, at ~ 3.4 arcmin from the nucleus. Here we refer to this as the ‘flare point’ (not to be confused with the inner jet flare point at around 14 arcsec from the nucleus: see H03). Ultraviolet emission is detected in the *GALEX* data both from this flare point and from regions of the jet closer to the nucleus.

Fig. 2 shows that the flare point is marked by a region of relatively strong X-ray emission which begins about 0.2 arcmin closer to the nucleus than the flare point and continues for about 1 arcmin. Thereafter almost no X-ray emission is seen from the jet, but the infrared emission continues. The X-ray region around the flare point (which we denote region G, following the notation of Feigelson et al. 1981) is resolved into several compact knots and extended emission. The compact knots are all closer to the nucleus than the flare point, but the brightest diffuse emission is coincident with the flare point, although the peak radio and infrared surface brightness (at about 3.5 arcmin) is offset from the peak X-ray surface brightness. This is illustrated by Fig. 3, which shows a profile along the jet in radio, infrared and X-ray. The fact that the infrared surface brightness begins to rise around knot G1 might imply that that the three knots are involved in high-energy particle acceleration, rather than being unrelated to the jet. There are no detected radio counterparts to these knots, but we do not have sensitive high-resolution radio data at this distance from the nucleus. The X-ray spectra of the knots are all well fitted with power laws with Galactic absorption ($N_H = 7 \times 10^{20}$ cm^{-2}) and have steep spectra (with photon indices of 1.84 ± 0.16, 2.01 ± 0.16, and 2.02 ± 0.23 respectively). However, their flux densities are low ($\sim$ 2 nJy each) and so they would not contribute significantly to the flux in the infrared if these spectra were extrapolated back to those frequencies.

In the absence of counterparts to the knots at other wavebands, we exclude them in what follows, and ask the question: is the overall spectrum of the *extended* emission consistent with a synchrotron model? To investigate this, we extracted flux densities from three matched regions of the jet around the flare point at all available frequencies, excluding point sources and, in the case of the X-ray, the compact knots labelled on Fig. 2, and measuring background from adjacent off-source background regions. The X-ray emission in these regions is dominated by the extended emission and so the exclusion of the knots makes little difference to our results. Fig. 1 shows the extraction regions, which we call the inner, middle and outer regions, and the results are tabulated in Table 1. The high background and low signal in the inner jet means that we cannot measure reliable fluxes for the inner jet at 8 and 4.5 μm. For the X-ray data, we fitted power laws with Galactic absorption to the two regions in which significant counts were detected to determine a 1-keV flux density (finding photon indices of 2.29 ± 0.05 and 2.44 ± 0.07 for the inner and middle regions respectively), and the upper limit to the flux density in the outer region was determined assuming a spectrum similar to that of the middle jet region. At other wavelengths the flux densities were determined by direct aperture photometry with background subtraction, excluding point sources. To first order, the two regions with detections in all wavebands are roughly consistent with the type of model we have fitted elsewhere (e.g. Hardcastle et al. 2001) in which the energy spectrum of all the electrons in the region is a broken power law with a non-standard break connecting the radio and X-ray and reproducing the X-ray photon indices; in this case the break must occur at energies lower than those corresponding to the infrared region (Fig. 4). However, in detail, the best-fitting infrared spectral indices (0.89 ± 0.25 and 0.84 ± 0.18 for the inner and middle regions respectively) are somewhat flatter than would be expected in this model, and the ultraviolet data points lie significantly above it, closer to a linear extrapolation from the infrared. In the middle region, in particular, where the *GALEX* fluxes are probably most reliable, the data appear to require a ‘bump’ above the best-fitting line in which the spectrum steepens and then flattens, which would imply a more complex electron population than our model allows for. The outer region, in which no significant ultraviolet or X-ray emission is detected, can also be fitted with a simple model, but in this case either the change of the electron spectral index, Δp, must be greater or there must be a cutoff in the electron spectrum between the infra-red and X-ray regions; the X-ray upper limit precludes fitting this region with a model identical to that used in the other two regions (Fig. 4). The best-fitting power law spectral index to the infrared data alone is 1.13 ± 0.19 for the outer region, which would be consistent with a larger Δp, though the errors are large. In such a model there may be low-level X-ray emission from this region that would be detectable in deeper observations.

No obvious jet-related infrared emission is seen on the counterjet side of the source. The counterjet radio and X-ray knots discussed by H03 are at small distances from the nucleus, where the infrared background from the host galaxy is high.

3.2 The small-scale jet

The Gemini observations do not detect any component of the jet within 24 arcsec of the nucleus. Using the baseline photometric calibration we estimate that an upper limit on any compact jet-like component is 1 mJy at 10 μm. The observations are less sensitive than would have been predicted, presumably because of the bright emission from the dust lane. The upper limit allows us to set a lower limit on the spectral index between radio and infrared, given the knot radio fluxes measured previously (H03), of $\alpha > 0.5$, consistent with the $\alpha_{\rm RI}$ measured for the large-scale jet, ~ 0.75. Since the knots in the inner region generally have steep X-ray spectral indices, it seems likely that their spectrum, like that of the outer jet, turns over before the infrared region. Sub-mm observations are required to test this.

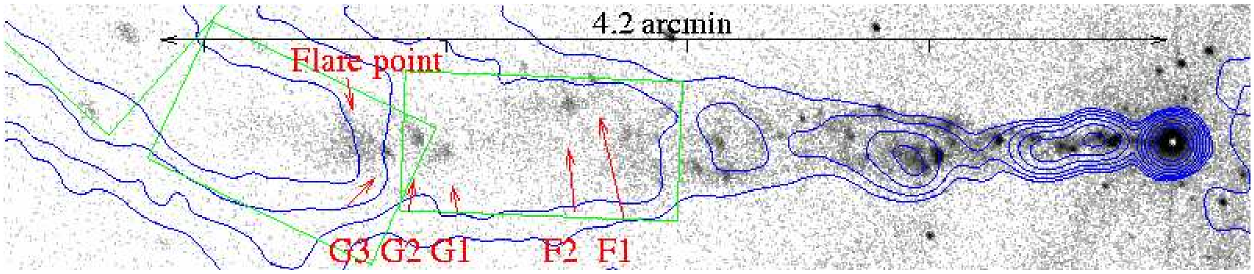

Figure 2. Unsmoothed *Chandra* greyscale image of the jet of Cen A in the 0.5-5.0 keV bands. Overlaid are the contours from Fig. 1. Pixels are the standard *Chandra* pixels, 0.492 arcsec on a side. Green boxes show (from right to left) the boundaries of inner, middle and outer extraction regions.

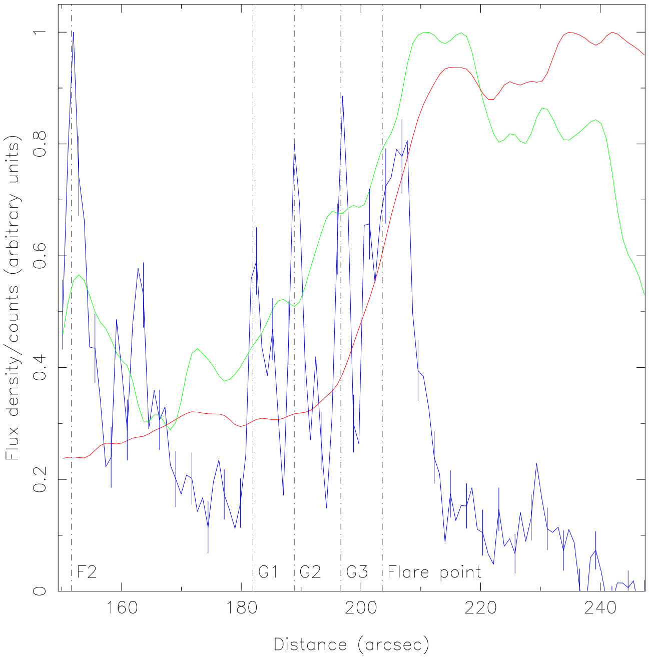

Figure 3. The profile of the part of the jet near the flare point. The x-axis shows linear distance from the nucleus along the jet. Red indicates radio emission (from a 4.9-GHz map with 6.2×2.0 arcsec resolution, beam elongated N-S), green indicates 24-μm infrared, and blue indicates 0.5-5.0 keV X-rays. The positions of the X-ray knots F2, G1, G2, G3 and of the flare point are marked with vertical lines. The extraction region for the profile was a rectangle 42 arcsec in the transverse direction: each point represents a 0.9-arcsec slice. Infrared and X-ray data were background-subtracted using adjacent identical regions. Representative Poisson errors are plotted on the X-ray points.

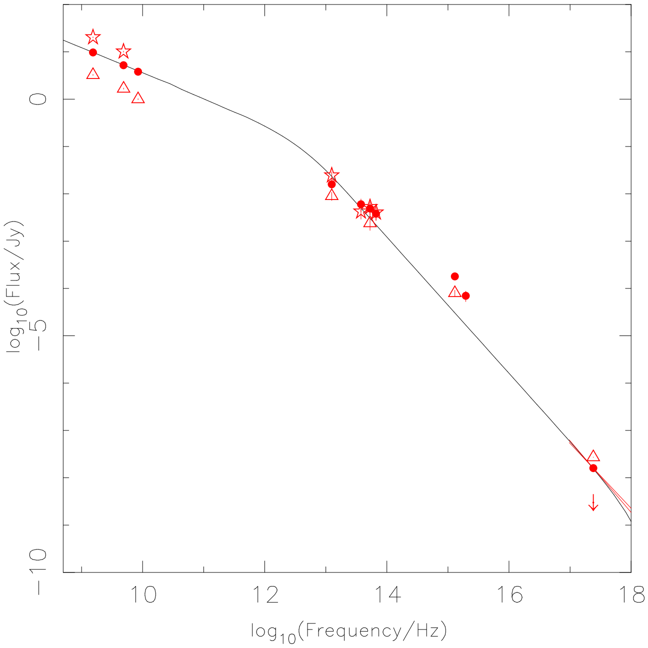

Figure 4. The spectra of the inner, middle and outer regions of the jet. Triangles denote the inner region, filled circles the middle region, and stars the outer region. The solid line is the best-fitting reference synchrotron model to the middle region, as described in the text. Where error bars are not visible they are smaller than symbols. The X-ray upper limit is marked with an arrow.

3.3 The nucleus

Cen A's nucleus has been observed at wavelengths around N-band by several other groups (Krabbe, Böker & Maiolino 2001; Karovska et al. 2003; Siebenmorgen, Krügel & Spoon 2004). We estimate the background-subtracted 10-μm flux density of the nucleus in our Gemini observations as 1.1 Jy, with a 10 per cent photometric calibration error. This is significantly higher than seen in some earlier observations, though consistent with the 1.5 ± 0.4 Jy reported by Karovska et al.from data taken in 2002 May, and may indicate variability on timescales of years. Variability has earlier been claimed at shorter infrared wavelengths (Turner et al. 1992). Comparing 825-s individual observations from 2004 Mar 06 with the short, 43-s observation of the standard star HD 110458, we find that the nucleus appears slightly resolved, with a Gaussian FWHM of 0.27 arcsec. Some of the apparent extension with respect to the PSF may be the result of the longer observation, with more chop/nod cycles, used for the nucleus, but we can conservatively say that the size of the nucleus at 10 μm is $\lesssim 0.27$ arcsec, or $\lesssim 4.5$ pc, consistent with the measurement of 0.17 ± 0.02 arcsec by Karovska et al. The torus in Cen A must thus be compact.

4 DISCUSSION: THE ORIGIN OF THE FLARE POINT

The *Spitzer* observations confirm that the broad-band spectrum of the large-scale Cen A jet can be described with a synchrotron model, as in other FRI sources, although the detailed spectral shape almost certainly requires a multi-component model for the synchrotron emission. However, the infrared detection points up the importance of the region we have called the flare point. Both the radio and infrared brighten by a factor ~ 3 here (Fig. 3) while there is little or no X-ray emission after the extended component of region G. The short synchrotron lifetime of X-ray-emitting electrons means that X-ray emission must always be associated with high-energy particle acceleration: but could the lack of X-rays after region G imply that this region, which is roughly coincident with the entry of the jet into the lobe, represents the 'last gasp' of particle acceleration in Cen A's jet? In a field strength of 3 nT, the equipartition value for this part of the jet, the electron energy loss timescale $(E/(\mathrm{d}E/\mathrm{d}t))$ is 2×10^4 years for electrons emitting at 4.5 μm, and 4×10^4 years for electrons emitting at 24 μm. The projected distance from the end of the X-ray emission at the flare point to the end of the jet, where only radio and 24-μm emission is detected, is roughly 2.5 kpc, implying a light travel time of $\sim 8 \times 10^3$ years. Thus, for particle acceleration to be absent in this region, we require jet speeds of $(0.2/\sin\theta)c$, where θ is the angle to the line of sight. As speeds in the inner jet are $\gtrsim 0.5c$, and the angle to the line of sight may be relatively large (see discussion in H03) this is not impossible, so that it could indeed be the case that significant high-energy particle acceleration ceases at the flare point.

This motivates us to ask a further question: what is the nature of the extended X-ray emission at the flare point? Most of the X-rays (Fig. 3) come from a region only 10 arcsec, or 170 pc, in size. This is still larger than the expected travel distance for 1-keV-emitting electrons (at most 100 pc) and in fact extended X-ray emission is seen on scales up to around 30 arcsec, making it difficult to sustain a model in which the particle acceleration here takes place at a single point if the magnetic field strength has its equipartition value, although only modest decreases in the magnetic field strength, by a factor of a few, would be necessary to make a one-shot acceleration model viable, since the loss timescale goes as $B^{-3/2}$. More puzzling in this picture is the offset between the peak X-ray, radio and infrared surface brightnesses seen in Fig. 3. It is also not clear what the physical relationship is between the diffuse X-ray emission at the flare point and the X-ray knots G1–3. In fact there is a striking similarity in the X-ray, albeit on larger scales, between the flare point and other regions in the inner part of the jet where we see compact X-ray features followed by diffuse X-ray emission, such as the region around knot BX2 (H03).

In H03 we argued that the knots in the inner jet were related to shocks as a result of interactions between the jet fluid and small-scale obstacles in the jet. The flare point is different in that it appears to affect the whole jet. It would be tempting, since the extended emission is associated with the entry of the jet into the high-surface-brightness regions of the NE lobe, to suggest that we are seeing an extended reconfinement shock, in which case the similarity of the length of the X-ray emitting region and the width of the radio jet implies a Mach number $\sim$ 2. The roughly tapering shape of the downstream X-ray emission is consistent with this idea (Sanders 1983) if only the inward-propagating shock accelerates particles to high energies. The idea that the jet decelerates rapidly and significantly at the flare point is consistent with the observation that it becomes both broader and brighter at this position. The details of the shock structure would then depend on the velocity structure of the jet, and it may be that a detailed model taking this into account could reproduce the offsets between the emission peaks at different frequencies. An alternative model is that the jet interacts at the flare point with some large-scale external feature that is able to affect the whole jet. Gopal-Krishna and Saripalli (1984) have pointed out the coincidence between the radio and X-ray flare point and an optical 'shell', seen in deep images, which they consider to be a remnant of a cannibalized galaxy. A series of shocks caused by such an interaction would be equally consistent with what we observe, if they can be distributed over the entire region of X-ray emission or, again, if the magnetic field is sub-equipartition.

Qualitatively, the bulk deceleration at the flare point in either of these scenarios is also consistent with the observed onset of bending of the jet there. However, if the jet really has a high bulk speed, as required to avoid *in situ* particle acceleration after the flare point, its density must be low. For example, if we assume that the jet is bent by the ram pressure of hot external material moving at the sound speed, then, applying Euler's equation (e.g. Eilek et al. 1984) and using the parameters of Kraft et al. (2003), the jet density must be 10^{-4} times the external density if the speed is $0.2c$. This is still a factor 5 above the minimum possible effective jet density (from the minimum-energy condition, assuming that the jet is a pure lepton/magnetic field plasma), but if any entrainment of baryonic material takes place in the inner jet, or if there is a significant departure from equipartion, the jet will be heavier, in which case relativistic bulk speeds at the bend would be unrealistic. In that situation, the post-shock jet speed would have to be slower, and some continuing *in situ* particle acceleration would be required to explain the extended infrared jet.

ACKNOWLEDGEMENTS

We are grateful to Charles Lawrence and Mairi Brookes for discussion of their results on Cen A prior to publication. MJH thanks the Royal Society for a research fellowship.

REFERENCES

Brodie, J.P., Königl, A., Bowyer, S., 1983, ApJ, 273, 154
Brookes, M.H., Lawrence, C.R., Stern, D., Werner, M., 2006, ApJ submitted
Cardelli, J.A., Clayton, G.C., Mathis, J.S., 1989, ApJ, 345, 245
Clarke, D.A., Burns, J.O., Norman, M.L., 1992, ApJ, 395, 444
Eilek, J.A., Burns, J.O., O'Dea, C.P., Owen, F.N., 1984, ApJ, 278, 37
Evans, D.A., Kraft, R.P., Worrall, D.M., Hardcastle, M.J., Jones, C., Forman, W.R., Murray, S.S., 2004, ApJ, 612, 786
Evans, D.A., Worrall, D.M., Hardcastle, M.J., Kraft, R.P., Birkinshaw, M., 2006, ApJ in press, astro-ph/0512600
Feigelson, E.D., Schreier, E.J., Delaville, J.P., Giacconi, R., Grindlay, J.E., Lightman, A.P., 1981, ApJ, 251, 31
Gopal-Krishna, Saripalli, L., 1984, A&A, 141, 61
Hardcastle, M.J., Birkinshaw, M., Worrall, D.M., 2001, MNRAS, 326, 1499
Hardcastle, M.J., Worrall, D.M., Kraft, R.P., Forman, W.R., Jones, C., Murray, S.S., 2003, ApJ, 593, 169 [H03]
Israel, F.P., 1998, A&A 8 237
Joy, M., Harvey, P.M., Tollestrup, E.V., Sellgren, K., McGregor, P.J., Hyland, A.R., 1991, ApJ, 366, 82
Kataoka, J., Stawarz, L., Aharonian, F., Takahara, F., Ostrowski, M., Edwards, P.G., 2006, ApJ in press, astro-ph/0510661
Krabbe, A., Böker, T., Maiolino, R., 2001, ApJ, 557, 626
Kraft, R.P., et al., 2000, ApJ, 531, L9
Kraft, R.P., Forman, W.R., Jones, C., Murray, S.S., Hardcastle, M.J., Worrall, D.M., 2002, ApJ, 569, 54
Kraft, R.P., Vázquez, S., Forman, W.R., Jones, C., Murray, S.S., Hardcastle, M.J., Worrall, D.M., Churazov, E., 2003, ApJ, 592, 129
Leeuw, L.L., Hawarden, T.G., Matthews, H.E., Robson, E.I., Eckart, A., 2002, ApJ, 565, 131
Neff, S.G., Schiminovich, D., Martin, C.D., 2003, AAS 203 96.07
Perlman, E.S., Biretta, J.A., Sparks, W.B., Macchetto, F.D., Leahy, J.P., 2001, ApJ, 551, 206
Sanders, R.H., 1983, ApJ, 266, 73
Schreier, E.J., Feigelson, E., Delvaille, J., Giacconi, R., Grindlay, J., Schwartz, D.A., Fabian, A.C., 1979, ApJ, 234, L39
Siebenmorgen, R., Krügel, E., Spoon, H.W.W., 2004, A&A, 414, 123
Turner, P.C., Forrest, W.J., Pipher, J.L., Shure, M.A., 1992, ApJ, 393, 648